

Coexistence of coagulation and streaming instabilities in protoplanetary discs

Arnaud Pierens¹, Thomas Collin-Dufresne¹, Min-Kai Lin^{2,3}, and Emmanuel DiFolco¹

¹ Laboratoire d'astrophysique de Bordeaux, Univ. Bordeaux, CNRS, B18N, allée Geoffroy Saint-Hilaire, 33615 Pessac, France
e-mail: arnaud.pierens@u-bordeaux.fr

² Institute of Astronomy and Astrophysics, Academia Sinica, Taipei 10617, Taiwan

³ Physics Division, National Center for Theoretical Sciences, Taipei City, 10617, Taiwan

December 17, 2025

ABSTRACT

The streaming instability is considered one of the leading candidates for the formation of planetesimals, due to its ability to overcome the bouncing and fragmentation barriers. The formation of dense dust clumps through this process, however, is possible provided it involves solids with dimensionless stopping times ~ 0.1 in standard discs, which typically corresponds to 1-10 cm-sized particles. This implies that dust coagulation is required for the SI to be an efficient process. Here, we employ unstratified, shearing-box simulations combined with a moment equation for solving the coagulation equation to examine the effect of dust growth on the SI. In dust-rich discs with a dust-to-gas ratio $\epsilon \gtrsim 1$, coagulation is found to have little impact on the SI; while in dust-poor discs with $\epsilon \sim 0.01$, we observe the formation of vertically extended filaments through the action of the coagulation instability (CI), which is triggered due to the dependence of coagulation efficiency on dust density. For moderate dust-to-gas ratios $\epsilon \sim 0.1$ and Stokes numbers $St \lesssim 0.1$, we find onset of the SI within these filaments, with a linear growth rate significantly higher compared to standard SI. We refer to this regime as coagulation-assisted SI. The synergy between both instabilities in that case leads to isotropic turbulence and dust concentrations that are increased by a factor of 30 – 40. As dust continues to grow, SI tends to overcome the effect of the CI such that the nonlinear saturation phase is similar to pure SI. Our results suggest that coagulation, by simply increasing dust size, may facilitate the formation of dense clumps through the SI; even though it has only little effect on its nonlinear evolution.

Key words. accretion, accretion discs – planet-disc interactions – planets and satellites: formation – hydrodynamics – methods: numerical

1. Introduction

In the standard scenario for planet formation, coagulation of micron-sized grains leads to the formation of millimeter-sized dust (Dullemond & Dominik 2005). Further growth of particles above the millimeter-size range is however rendered difficult because of the bouncing (Zsom et al. 2010) and fragmentation (Zsom et al. 2010) barriers. An emerging picture to overcome these barriers is that 100-km sized planetesimals form directly through the streaming instability (hereafter SI; Youdin & Goodman (2005); Youdin & Johansen (2007)) that occurs as a result of angular momentum exchange between the gas and dust components, and rotation. It has been shown that during the nonlinear evolution of the SI, dust particles can eventually directly concentrate into clumps or filaments, which can subsequently become gravitationally unstable to form 100-1000 km-sized bodies (Johansen et al. 2009; Simon et al. 2016; Abod et al. 2019). The ability for solids to experience a regime of strong clumping depends mainly on the dimensionless stopping time St and local dust-to-gas ratio ϵ , which can also be quantified through the dust-to-gas surface density ratio $Z = \Sigma_d/\Sigma_g$ where Σ_d (resp. Σ_g) is the dust (resp. gas) surface density. For $Z \sim 5 \times 10^{-3}$, strong clumping requires $St \gtrsim 0.1$ in a disc where no external turbulence operates, whereas for $St \lesssim 0.01$ strong clumping is triggered for a critical solid abundance of a few percent (Carrera et al. 2015; Yang et al. 2017; Li & Youdin 2021). In any case, this suggests

that a level of dust growth is needed for the SI to enter the strong clumping regime (Drążkowska & Dullemond 2014).

Taking into account the effect of dust growth on the SI in a self-consistent fashion is however a difficult task. The process of dust growth is indeed expected to be a sensitive function of the relative collision velocity between grains, which depends on many processes operating in the protoplanetary disc. As a consequence, the resulting dust size distribution is not known a priori and remains uncertain. The generalization of the classical, monodisperse SI to multiple dust sizes have nevertheless been examined by a number of recent studies, but adopting prescribed dust size distributions. These have shown that the growth rate of the polydisperse, multispecies SI (PSI) tends to decrease as the number of species is increased (Krapp et al. 2019), and becomes very small in the limit of a continuous size distribution (Paardekooper et al. 2020; Zhu & Yang 2021). However, it was also found that a top-heavy size distribution, resulting for instance from a pure coagulation process, leads to PSI linear growth rates equivalent to those of the classical SI (McNally et al. 2021).

The influence of the process of coagulation itself on the nonlinear development of the monodisperse SI has been investigated by Ho et al. (2024) using stratified simulations. These authors found that coagulation tends to broaden the range of Stokes numbers and dust-to-gas ratios over which the SI can be triggered, due to ability for coagulation to promote dust growth. Conversely, it has even been proposed that dust growth can be sig-

nificantly boosted in the strong clumping regime of the SI (Tominaga & Tanaka 2023, 2025). This arises because dust-loading increases the inertia of the dusty fluid, resulting in a reduction of the effective sound speed and lower collision velocities between dust grains. These results suggest that a feedback loop between coagulation and the development of the SI may exist, and this has been recently studied by Carrera et al. (2025).

In this paper, we examine the effect of the coagulation instability (hereafter CI) on the linear growth and nonlinear saturation phase of the SI (Tominaga et al. 2021). The coagulation instability is a consequence of the interplay between the dust coagulation process and radial drift of dust particles, and is primarily related to the dependence of mass growth rate on dust density. As described by Tominaga et al. (2021), if one assumes a positive dust density perturbation, the resulting increased coagulation efficiency leads to a variation of the dust size. This subsequently causes an enhanced radial drift speed which tends to amplify the initial density perturbation, resulting in a feedback loop. It has been shown that the nonlinear evolution of the CI can enable the Stokes number of solids to rapidly reach unity, even for relatively modest dust-to-gas ratios $\epsilon \sim 10^{-3}$ (Tominaga et al. 2022a,b). Therefore, the CI may represent a promising mechanism to extend the parameter space (in terms of dust-to-gas ratios and Stokes numbers) over which the SI can operate efficiently.

To investigate the possible effect of the CI on the SI in more detail, we perform 2D axisymmetric, unstratified, shearing-box simulations in which coagulation is modelled using the single-size approximation. Our main aims are to i) assess whether the CI can help the SI enter the regime of strong clumping and ii) evaluate to what extent the turbulence driven by the CI subsequently impacts the nonlinear development of the SI.

The paper is organized as follows. In Sect. 2, we present the governing evolution equations of the gas and dust components. We then describe in Sect. 3 the numerical setup and the initial conditions that are used in the simulations, whose results are presented in Sect. 4. We discuss our results in Sect. 5 and present a summary of our findings in Sect. 6.

2. Physical model

2.1. Governing equations

We model a local patch in a protoplanetary disk within the shearing box framework. A cartesian coordinate system with origin located at an arbitrary distance R_0 from the central star corotates with angular velocity $\Omega_0 = \Omega_k(R_0)$, with Ω_k the Keplerian angular velocity. The x- and y- axes are oriented radially outward and along the orbital direction respectively, while the z-axis is directed in the vertical direction. We assume that the domain is small compared to the orbital distance so that Keplerian rotation appears as a linear shear flow with velocity $\mathbf{U}_k = -\frac{3}{2}x\Omega_0\hat{\mathbf{y}}$. We assume the system is axisymmetric and neglect the vertical component of stellar gravity. In these limits, the continuity and momentum equations for the gas and dust components are respectively given by:

$$\frac{\partial \rho_g}{\partial t} + \nabla \cdot (\rho_g \mathbf{u}) = 0 \quad (1)$$

$$\begin{aligned} \frac{\partial \mathbf{u}}{\partial t} + \mathbf{u} \cdot \nabla \mathbf{u} = 2u_y\Omega\hat{\mathbf{x}} - u_x\frac{\Omega}{2}\hat{\mathbf{y}} - \frac{1}{\rho_g}\nabla P + 2\eta R\Omega^2\hat{\mathbf{x}} + \frac{\epsilon}{\tau_s}(\mathbf{v} - \mathbf{u}) \\ + \frac{1}{\rho_g}\nabla \cdot \mathbf{T} \quad (2) \end{aligned}$$

$$\frac{\partial \rho_d}{\partial t} + \nabla \cdot (\rho_d \mathbf{v}) = \nabla \cdot (D\rho_d \nabla \epsilon) \quad (3)$$

$$\frac{\partial \mathbf{v}}{\partial t} + \mathbf{v} \cdot \nabla \mathbf{v} = 2v_y\Omega\hat{\mathbf{x}} - v_x\frac{\Omega}{2}\hat{\mathbf{y}} - \frac{1}{\tau_s}(\mathbf{v} - \mathbf{u}) \quad (4)$$

where ρ_g and ρ_d are the gas and dust densities respectively, and \mathbf{u} , \mathbf{v} their velocities measured relatively to the background Keplerian shear. We adopt an isothermal equation of state $P = \rho_g c_s^2$ where $c_s = H_g \Omega_0$ is the (constant) sound speed with H_g the gas pressure scale height. In Eq. 2, \mathbf{T} is the viscous stress tensor which is given by:

$$\mathbf{T} = \rho_g \nu \left(\nabla \mathbf{u} + (\nabla \mathbf{u})^\dagger - \frac{2}{3} I \nabla \cdot \mathbf{u} \right) \quad (5)$$

where ν is the kinematic viscosity which is employed to model the effects of possible underlying turbulence. Regarding the resulting turbulence-induced particle stirring, it is modeled by the source term appearing in the dust continuity equation, where D is the dust diffusion coefficient which is set here to $D = \nu$. It is important to note that viscosity and diffusion are generally not included in our simulations, except in those presented in B.

In Eq. 2, the term $\propto \eta$ corresponds to an outward force acting on the gas due to a background radial pressure gradient, and determined by the dimensionless parameter:

$$\eta = -\frac{1}{2\rho_g \Omega_0^2 R_0} \frac{\partial P}{\partial r} \quad (6)$$

Finally, τ_s is the stopping time that we will characterize in the following in terms of the dimensionless Stokes number $St = \tau_s \Omega$. Dust grains are assumed to be in the Epstein regime such that St is the related to the grain size a through:

$$St = \sqrt{\frac{\pi}{8}} \frac{\rho_i a}{\rho_g c_s} \Omega \quad (7)$$

where ρ_i is the internal density of dust grains, and $m = 4\pi\rho_i a^3/3$ their mass. In this work, we allow m (and consequently a) to increase as a result of dust coagulation, which we model here using a single-size approximation (Sato et al. 2016; Tominaga et al. 2021). This consists in following the size evolution of grains whose mass m_p dominate the dust density distribution at each location. The evolution equation for the so-called peak mass m_p can be obtained by considering the first-moment of the Smoluchowski equation (e.g. Tominaga et al. (2021), Appendix A), and it reads:

$$\frac{\partial m_p}{\partial t} + \mathbf{v} \cdot \nabla(m_p) = \mathcal{S}^+(St_p) - \mathcal{S}^- \quad (8)$$

where $\mathcal{S}^+ = 4\pi a_p^2 \Delta v_{pp} \rho_d$ with a_p the grain size corresponding to m_p , and Δv_{pp} the typical relative velocity between particles, is the mass growth rate resulting from coagulation, and which can generally be expressed as a function of the Stokes number St_p corresponding to m_p . Although dissipation effects are not included in our dynamical equations, we follow Tominaga et al. (2021) and assume that relative velocities are dominated by the turbulence experienced by the disc. This allows us to i) make the problem analytically tractable and ii) identify clearly the role played by coagulation. In that case, and in the limit $St \ll 1$, we

can further make use of a simplified expression for Δv_{pp} given by (Ormel & Cuzzi 2007):

$$\Delta v_{\text{pp}} = \sqrt{C \text{St}_p \alpha_{\text{coag}} c_s}; \quad (9)$$

where C is a numerical factor set to $C = 2.3$, and α the dimensionless turbulent stress parameter (Shakura & Sunyaev 1973) which is here fixed to $\alpha_{\text{coag}} = 10^{-4}$. In the following and for convenience, we will simply drop the subscript p in the definition of St_p and a_p such that, unless otherwise stated, $\text{St} = \sqrt{\frac{\pi}{8} \frac{\rho_i a}{\rho_g c_s}} \Omega$ with $\rho_i = 3m_p/4\pi a^3$.

With respect to the original work of Tominaga et al. (2021), we include in the mass evolution equation Eq. 8 an additional, *constant* sink term \mathcal{S}^- whose value is set to the initial value of \mathcal{S}^+ . The primary aim of adding this term is to ensure that the initial chosen particle mass corresponds to an equilibrium solution to the set of Eqs. 1-4, combined with Eq. 8. Given that the radial and vertical dependences of equilibrium quantities are ignored in the box, the left-hand side of Eq. 8 becomes zero at steady-state, leading therefore to $\mathcal{S}^- = \mathcal{S}^+$.

We notice that in principle, dust loading leads to a reduction of the sound speed by increasing the inertia of the dusty fluid. This can be expressed by defining an effective sound speed given by (Lin & Youdin 2017):

$$\tilde{c}_s = \frac{c_s}{\sqrt{1 + \epsilon}} \quad (10)$$

From Eq. 9, a reduction in the sound speed due to dust-loading results in a decrease of the collision velocity. Recent work has shown that this effect may cause rapid dust growth in the strong clumping regime of the SI, due to the significant increase in the local dust-to-gas ratio there (Tominaga & Tanaka 2023, 2025; Carrera et al. 2025). Here, we do not account for this potential important effect and simply employ the nominal sound speed when computing the collision velocity.

2.2. Equilibrium state

For constant values of ρ_g , ρ_d and St , equilibrium solutions to Eqs. 1-4 can be obtained, leading to velocity deviations from Keplerian rotation given by:

$$u_x = \frac{2\epsilon \text{St}}{\Delta^2} \eta R_0 \Omega, \quad (11)$$

$$u_y = -\frac{(1 + \epsilon + \text{St}^2)}{\Delta^2} \eta R_0 \Omega, \quad (12)$$

$$v_x = \frac{-2\text{St}}{\Delta^2} \eta R_0 \Omega, \quad (13)$$

$$v_y = -\frac{(1 + \epsilon)}{\Delta^2} \eta R_0 \Omega, \quad (14)$$

where $\Delta^2 = \text{St}^2 + (1 + \epsilon)^2$. For a fixed grain size, these correspond to the traditional steady-state drift solutions for a dusty disc obtained by Nakagawa et al. (1986). As mentioned above, including coagulation is not expected to impact these equilibrium solutions, due to the presence of the sink term in the right-hand side of Eq. 8.

3. Methodology

3.1. Numerical method and model setup.

We examine the nonlinear dynamical evolution of the system by performing 2.5D (axisymmetric), unstratified simulations in a shearing-box using the multifluid version of the publicly available code FARGO3D (Benítez-Llambay & Masset 2016; Benítez-Llambay et al. 2019). We considered single dust species runs in which the effect of coagulation was implemented in the aforementioned single-size approximation, albeit using a conservative version of Eq. 8:

$$\frac{\partial m_p \rho_d}{\partial t} + \nabla \cdot (m_p \rho_d \mathbf{v}) = p_{\text{eff}} (\mathcal{S}^+ - \mathcal{S}^-) \rho_d \quad (15)$$

Under this form, the previous equation can be integrated using the operator splitting technique employed by FARGO3D, with a coagulation term solved as a new substep within the source step. Tests of the implementation are presented in Appendix A. With respect to Eq. 8, the previous expression includes an additional, sticking efficiency, term p_{eff} whose expression is similar to that used by Tominaga et al. (2022a):

$$p_{\text{eff}} = \min \left(1, -\frac{\ln(\text{St}/\text{St}_f)}{\ln 5} \right), \quad (16)$$

and which prevents the value for the Stokes number to increase above St_f . This enables to i) take into account the effect of the fragmentation process in the simulations and ii) examine the evolution outcome as a function of parameter St_f .

In our shearing-box setup, the cartesian coordinate system is oriented with x along the (outward) radial direction and z pointing along the (upward) vertical direction. The domain considered is such that $x \in [-0.0125, 0.0125]$ and $z \in [-0.0025, 0.0025]$, or equivalently $x \in (-0.25, 0.25)H_0$ and $z \in (-0.05, 0.05)H_0$. The appropriate size of the shearing-box was determined from convergence tests but typically, a large radial extent of the domain is needed to accommodate the most unstable wavelength expected from linear growth maps of the streaming instability as $\text{St} \rightarrow \text{St}_f$, whereas the small vertical extent of the domain is consistent with an unstratified setup, focusing on the disc midplane. The domain is covered by $N_x \times N_z = 2048 \times 512$ grid cells, with the radial resolution chosen as to capture the largest number of CI unstable modes, as these have growth rates increasing with radial wavenumber in absence of diffusive processes.

As we do not consider the vertical gravity in this work, boundaries are taken to be periodic in the z -direction, while we use standard shearing periodic boundaries in x .

3.2. Parameters and initial conditions

We adopt a unique value for the pressure gradient parameter $\eta = 0.005$, corresponding to a typical pressure gradient in a protoplanetary disc. Three values of the initial dust-to-gas mass ratio ϵ are considered, $\epsilon = 0.02, 0.2, 3$, which are representative of low ($\epsilon = 0.02$), moderate ($\epsilon = 0.2$), and high dust abundances ($\epsilon = 3$). For simulations in which dust coagulation is discarded, the Stokes number is kept constant with values: $\text{St} = 0.01, 0.1, 1$; whereas in those including coagulation the Stokes number is computed from Eq. 15, starting from an initial value $\text{St}_i = 10^{-3}$. Details of parameters for each simulation are presented in Table 1.

Regarding the initial conditions, radial and azimuthal components of dust and gas velocities are initialized according to Eqs. 11-14, while setting the vertical component to zero. In most

Table 1. Summary of parameters adopted in our runs.

Run label	Coagulation	St_f	ϵ	α_{SS}	$\alpha_{g,x}$	$\alpha_{g,y}$	$\alpha_{g,z}$	$\tau_{c,x}$	$\tau_{c,y}$	$\tau_{c,z}$
E0v02S0v01	no	10^{-2}	0.02	-4.85e-07	1.12e-09	3.57e-12	1.60e-12	0.14	1.53	0.34
E0v02S0v01c	yes	10^{-2}	0.02	-9.45e-7	2.80e-7	3.06e-8	3.40e-7	0.12	0.18	0.22
E0v02S0v1	no	10^{-1}	0.02	-4.80e-6	1.12e-9	2.73e-11	2.42e-13	0.10	1.37	0.42
E0v02S0v1c	yes	10^{-1}	0.02	-8.55e-6	1.09e-7	5.11e-8	3.42e-6	0.09	0.17	0.12
E0v02S1	yes	1	0.02	-4.75e-5	3.04e-7	5.19e-7	2.06e-6	0.10	0.11	0.3
E0v02S1c	yes	1	0.02	-3.46e-5	8.89e-8	2.24e-7	7.92e-7	0.09	0.10	0.12
E0v2S0v1	no	10^{-1}	0.2	-5.5e-5	1.25e-8	1.26e-8	1.5e-8	0.16	0.19	0.17
E0v2S0v1c	yes	10^{-1}	0.2	-1.06e-4	5.39e-6	1.31e-5	9.87e-6	0.09	0.09	0.11
E0v2S0v01	no	10^{-2}	0.2	-5.78e-6	1.17e-9	8.2e-11	6.33e-11	0.11	1.46	0.26
E0v2S0v01c	yes	10^{-2}	0.2	-7.19e-6	2.15e-7	5.34e-7	5.63e-7	0.10	0.13	0.16
E0v2S1	no	1	0.2	-3.43e-4	5.61e-6	9.68e-6	6.93e-6	0.14	0.16	0.14
E0v2S1c	yes	1	0.2	-3.43e-4	5.29e-6	8.62e-6	6.41e-6	0.14	0.14	0.13
E3S0v01	no	10^{-2}	3	-3.43e-4	5.61e-6	9.68e-6	6.93e-6	0.17	0.24	0.09
E3S0v01c	yes	10^{-2}	3	-7.19e-6	2.15e-7	5.34e-7	5.63e-7	0.18	0.10	0.23
E3S0v1	no	10^{-1}	3	-1.1e-4	7.44e-06	7.89e-06	5.37e-06	0.08	0.24	0.13
E3S0v1c	yes	10^{-1}	3	-1.1e-4	8.90e-06	8.18e-06	5.79e-06	0.08	0.26	0.13
E3S1	no	1	3	-5.1e-6	9.52e-06	1.32e-05	4.37e-06	0.11	0.26	0.3
E3S1c	yes	1	3	-5.1e-6	9.58e-06	1.32e-05	4.3e-06	0.08	0.24	0.13

runs, the initial dust velocities are then seeded with random noise of amplitude $10^{-2}c_s$. Because the effects of stratification are not considered, we use an initial gas density $\rho_0 = 1$. We also use a system of units in which $c_s = \Omega_k = H_g = 1$.

3.3. Diagnostics

One aim of this work is to assess the level of turbulence generated by the coagulation and streaming instabilities. To quantify the flux of angular momennum carried by turbulence, we first define the Shakura-Sunyaev stress parameter (Shakura & Sunyaev 1973):

$$\langle \alpha_{SS} \rangle = \frac{\langle \rho_g u_x u_y \rangle}{\rho_0 c_s^2}, \quad (17)$$

where the symbol $\langle \rangle$ denotes averaging in the x-z plane. To obtain a reliable measure of α_{SS} , we further perform a time average of the latter quantity, and given by:

$$\overline{\langle \alpha_{SS} \rangle} = \frac{1}{t_2 - t_1} \int_{t_1}^{t_2} \langle \alpha_{SS} \rangle dt \quad (18)$$

which we typically compute over a time interval of $\Delta t = t_2 - t_1 \sim 10\Omega^{-1}$ once saturation has been attained. We also measure the velocity dispersion of the gas $\delta \mathbf{u}$ whose i th component is given by:

$$\delta u_i = \sqrt{\langle u_i^2 \rangle - \langle u_i \rangle^2}, \quad (19)$$

and the autocorrelation time $t_{c,i}$ of the velocity fluctuations, which is obtained by evaluating each component of the autocorrelation function given by (Yang et al. 2018):

$$\mathcal{R}_i(t) = \int [u_i(\tau) - \bar{u}_i][u_i(t + \tau) - \bar{u}_i]d\tau \quad (20)$$

In the previous expression, \bar{u} is the mean velocity, whose components u_i are estimated by considering their time average in the interval $[t_1, t_2]$:

$$\bar{u}_i = \frac{1}{t_2 - t_1} \int_{t_1}^{t_2} u_i(\tau) d\tau \quad (21)$$

Following Hsu & Lin (2022), we set $t_2 - t_1 = 5P$ and record the data with a cadence of $0.01P$ (Yang et al. 2018) to compute Eq. 20. We then determine $t_{c,i}$ by fitting an exponential function to the autocorrelation function (Fromang & Papaloizou 2006).

From Eqs. 19 and 20, we can subsequently compute the gas bulk diffusion coefficient $D_{g,i}$ in the i th direction and which is given by:

$$D_{g,i} = \overline{\delta u_i^2} t_{c,i} \quad (22)$$

In the following, we will rather make use of the dimensionless bulk gas diffusion coefficient, defined by:

$$\alpha_{g,i} = \frac{D_{g,i}}{c_s H_g} = \left(\frac{\overline{\delta u_i^2}}{c_s} \right)^2 \tau_{c,i} \quad (23)$$

where $\tau_{c,i}$ is the dimensionless equivalent of the correlation time:

$$\tau_{c,i} = t_{c,i} \Omega_0^{-1} \quad (24)$$

4. Results

In this section, we discuss the impact of dust coagulation on the non-linear evolution of the SI by providing a systematic comparison between pure SI simulations and runs that include dust coagulation. Our comparison rely on models in which the maximum Stokes number St_f coincides with the value for St set in standard SI simulations. For simplicity, we will therefore simply denote St_f as St when presenting the results of the simulations.

In Fig. 1 we present an overview of the results where we show the time evolution of the maximum dust-to-gas ratio ϵ_{max} and Stokes number St for each model we considered. From this figure, it is immediately obvious that in dust rich discs, the impact of coagulation is relatively weak as simulations that include this effect reach overdensities that are very similar to those obtained in standard SI simulations.

In dust-poor discs with $\epsilon < 0.2$, however, including coagulation has a stronger effect, with overdensities that can be a factor

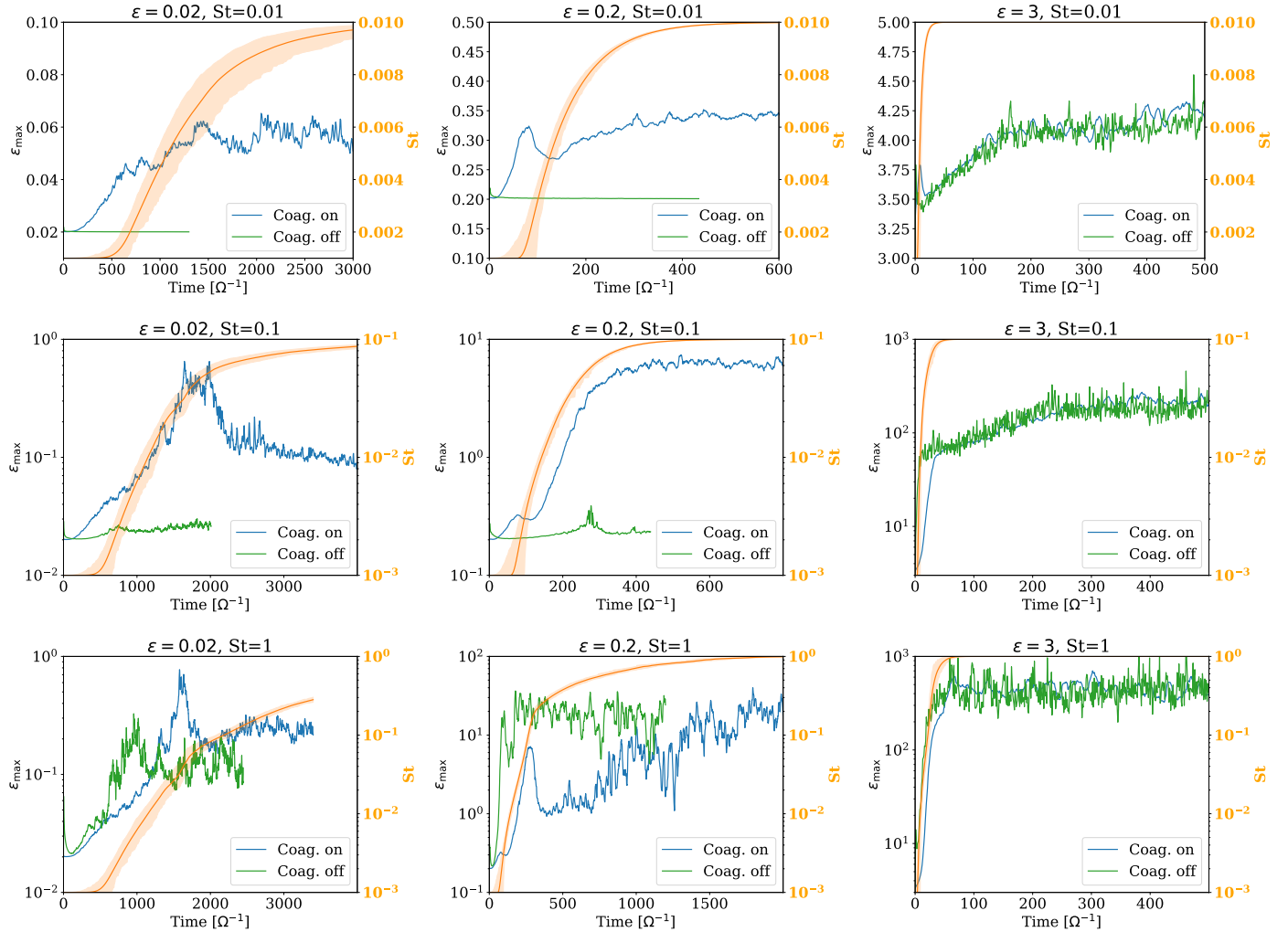


Fig. 1. Time evolution of the maximum dust-to-gas ratio ϵ_{\max} and Stokes number for all simulations listed in Table 1. The left, middle, right columns correspond to $\epsilon = 0.02, 0.2, 3$ respectively while the upper, middle, and lower panels correspond to $St = 0.01, 0.1, 1$ respectively. In each panel, we show the evolution of ϵ_{\max} for the case with (blue) and without (green) coagulation. For the evolution of St , the light colour traces the minimum and maximum values whereas the dark colour traces the box averaged value.

of 5 – 30 higher than without coagulation for tightly coupled particles. In this regime, we find that the coagulation instability (hereafter CI; Tominaga et al. (2021)) plays an important role in the evolution, as it is found to dominate over other processes for $\epsilon = 0.02$, or even interact with the SI for $\epsilon = 0.2$. Below, we describe in more details these two different modes of evolution found for Stokes numbers $St < 0.1$. We then discuss the case of marginally coupled particles with $St \approx 1$.

4.1. Tightly coupled particles

4.1.1. $\epsilon = 0.02$: Evolution mediated by CI

The CI is by essence a dust-driven instability which involves two ingredients: i) the dust-density density dependence of the collisional coagulation rate and ii) the dependence of St with the particle size. When these are mixed, a dust surface density perturbation $\delta\Sigma_d$ leads to a radial variation of St , resulting in a traffic jam which tends to enhance $\delta\Sigma_d$. Compared to other dust-driven instabilities, the CI can develop over a few orbital periods even for small dust-to-gas ratios $\epsilon \sim 10^{-3}$. More precisely, the growth

rate of the CI is typically given by (Tominaga et al. 2021):

$$\sigma = \sqrt{\frac{1}{2} \frac{\epsilon}{3t_0} k} < v_x > |\Omega^{-1}| \quad (25)$$

where k is the radial wavenumber, and v_x is given by Eq. 13. $t_0 = 4/3 \sqrt{2St_i/aC\pi}$ is the mass growth timescale of a dust particle and can be obtained from Eq. 8. For $St_i = 10^{-3}$ and $\epsilon = 0.02$, and setting $kH = 4 \times 10^3$ which corresponds to the maximum wavenumber that is resolved by ≈ 6 grid cells, we get $\sigma \approx 2.10^{-3}\Omega^{-1}$. The time evolution of the maximum dust-to-gas ratio and Stokes number is shown, for $\epsilon = 0.02$ and $St = 0.01$ (Model E0v02S0v01c), in the upper left panel of Fig. 1. Both quantities exhibit an initial rapid exponential growth phase and then reach non-linear saturation at $t \sim 1500\Omega^{-1}$. We note in passing that in the context of the CI, unstable modes are essentially incompressible such that the evolution of ϵ_{\max} reflects the evolution of the maximum of the perturbed dust density $\delta\rho_d$. From this plot, we estimate a linear growth rate of $\sigma \sim 1.7 \times 10^{-3}\Omega^{-1}$ during the initial linear growth phase, which is in good agreement with our previous analytical estimation. This clearly indicates that the CI is responsible for the initial increase in $\delta\rho_d$ and St that are observed, although disentangling the effect of the CI from the

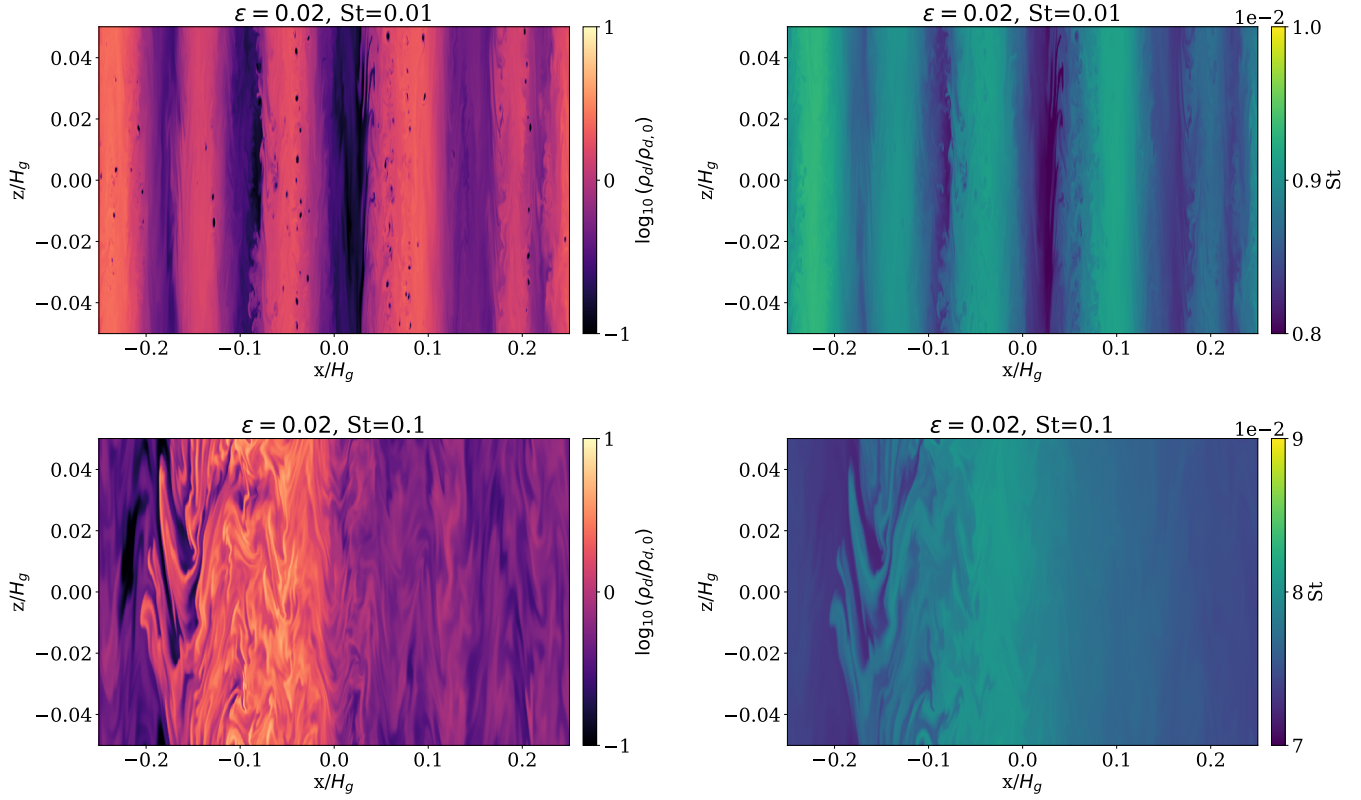


Fig. 2. In the case $\epsilon = 0.02$, snapshots of the dust density (left) and Stokes number (right) for model E0v02S0v01c with $St = 0.01$ (left), and model E0v02S0v1c with $St = 0.1$ (right). Both models include the effect of coagulation and result in the growth of the coagulation instability.

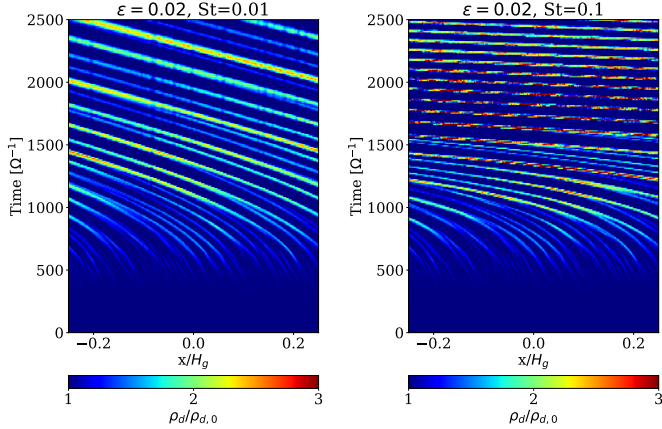


Fig. 3. In the case $\epsilon = 0.02$, time evolution of the vertically averaged dust density for model E0v02S0v01c with $St = 0.01$ (left), and model E0v02S0v1c with $St = 0.1$ (right).

evolution of the averaged Stokes number is more difficult. For such small values of ϵ and St , we also note that the effect of the SI is expected to be negligible, and this is confirmed by inspecting the evolution for the case where coagulation is switched off (green line), and for which ϵ_{max} remains close to its initial value.

Fig. 2 shows snapshots of the dust density and Stokes number at saturation, for this model and in the case with $\epsilon = 0.02$ and $St = 0.1$ (Model E0v02S0v1c) for which a similar mode of evolution is found. Since the CI is originally a one-dimensional instability with no dependence in the vertical direction, it is not surprising to observe the formation of vertically extended filaments, whose number tends to decrease as St is increased. For

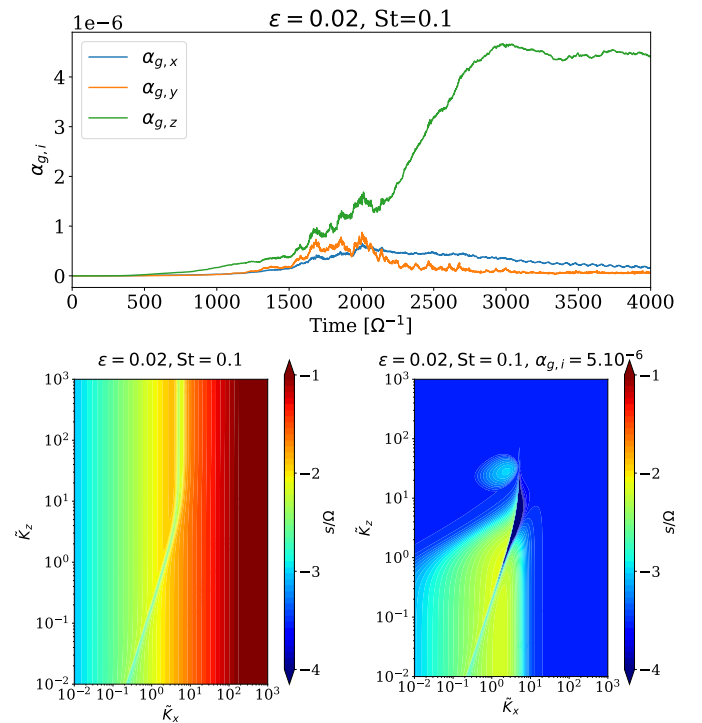


Fig. 4. For $\epsilon = 0.2$ and $St = 0.01$ (model E0v02S0v01c), time evolution of the dimensionless diffusion coefficients $\alpha_{g,i}$ in each direction (top). The lower panel shows expected linear growth rates for the same model in the inviscid case (left) and for $\alpha_{g,i} = 5 \times 10^{-6}$ (right). These have been obtained from linear theory (see App. A) using $D = \nu = \alpha_{g,i} c_s H_g$. Here, $\tilde{k}_{x,z} = k_{x,z} \eta R_0$ are the dimensionless wavenumbers.

$St = 0.1$, we indeed ultimately obtain a single filament with $\epsilon_{max} \approx 0.1$ whereas for $St = 0.01$, five filaments remain in the system at the end of the simulation with consequently smaller $\epsilon_{max} \approx 0.006$. We find that these filaments are themselves formed through the merging of thinner ones. This is illustrated in Fig. 3 where we display the vertically-averaged dust density as a function of time and radial position. From this figure, it is clear that filaments grow not only via merging events but also by simply collecting dust as they drift inward. Both effects then combine to make the amplitude of the perturbed dust density start level off and saturate at later times. Another mechanism that may contribute to saturation is the level of turbulence generated by the CI itself. This is suggested by looking back to Fig. 2 where it is evident that turbulence operates in the disc, especially for $St = 0.1$. For this case, the time evolution of the dimensionless bulk gas diffusion coefficients $\alpha_{g,i}$ is shown in the upper panel of Fig. 4. Not surprisingly, this reveals anisotropy of the CI with an enhanced dust diffusion coefficient $\alpha_{g,z}$ of $O(10^{-6})$ in the vertical direction, which is larger by two orders of magnitude compared to $\alpha_{g,y}$. A similar trend is also found for $St = 0.01$ (see Table 1), with $\alpha_{g,z}$ of $O(10^{-7})$ and $\alpha_{g,y}$ of $O(10^{-8})$ in that case. The bottom panel of Fig. 4 compares linear growth rates for $\alpha_{g,i} = 0$ (left) and for $\alpha_{g,i} = 3 \times 10^{-6}$ (right), and which have been obtained from the linearized equations presented in Appendix A using $\nu = D = \alpha_{g,i} c_s H_g$. We see that the turbulent diffusion induced by the CI itself can indeed significantly cut off the most unstable modes corresponding to $\alpha_{g,i} = 0$. Although not shown here, we find a similar effect for $St = 0.01$, which confirms that the CI-induced dust diffusion can also contribute to the saturation of the instability.

In summary, we find that for tightly coupled particles, the CI can operate in dust-poor discs and lead to the formation of dust rings with ϵ_{max} of $O(0.1)$, which is, however, not enough to subsequently trigger the SI within these rings. This is because the dust backreaction onto the gas tends to significantly regulate the maximum dust concentration that can be achieved through the CI (Tominaga et al. 2022b). This is illustrated in Fig. 5 where we show the time evolution of the maximum dust-to-gas ratio and Stokes number for the same models that include dust coagulation, but in the case where the effect of the dust backreaction onto the gas is discarded. We find a significantly higher ϵ_{max} in that case, consistently with the results of Tominaga et al. (2022b) (see their Figure 3.).

4.1.2. $\epsilon = 0.2$: Interplay between CI /SI and turbulence

In the case with $\epsilon = 0.2$, we find that the difference in amplitude between the $\alpha_{g,i}$ coefficients is smaller. For simulations including coagulation, their time evolution is represented in Fig. 6. The underlying turbulence is more isotropic in that case, with $\alpha_{g,y} \sim \alpha_{g,z}$ for both $St = 0.01$ (Model E0v2S0v01c) and $St = 0.1$ (Model E0v2S0v1c). This is also illustrated in Fig. 7 where we plot the kinetic energy spectrum at saturation for $St = 0.1$. The power spectrum is broadly consistent with a negative five third power law (dashed line), which suggests Kolmogorov-like turbulence. Isotropic turbulence is expected for classical SI-driven turbulence, although we find an early evolution driven by the CI. In Fig. 1, the top-middle and middle-middle panels show the evolution for $St = 0.01$ and $St = 0.1$ respectively. For models with coagulation, the initial rise in ϵ_{max} (for $t \lesssim 100 \Omega^{-1}$ typically) is caused by the CI, involving density growth of vertically extended filaments through dust capture and merging of these filaments into denser ones. Compared to the previous case with $\epsilon = 0.02$,

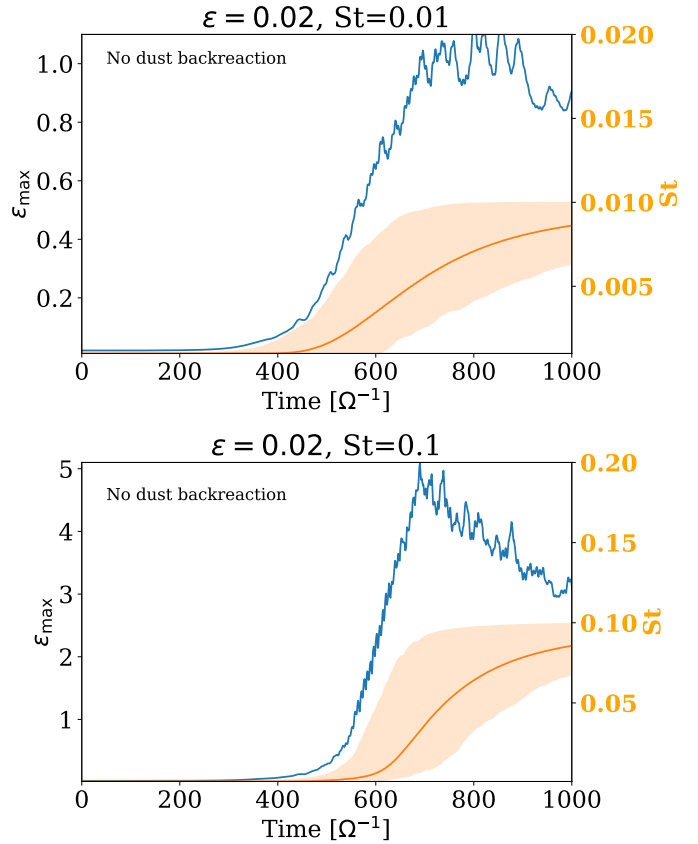


Fig. 5. For $\epsilon = 0.2$, time evolution of the maximum dust-to-gas ratio ϵ_{max} and Stokes number for $St = 0.01$ (top) and $St = 0.1$ (bottom), in the case where the effect of the dust backreaction onto the gas is discarded.

however, it appears that the value for ϵ_{max} is high enough to trigger the SI within the filaments, which leads to the subsequent increase in ϵ_{max} that is observed. This would be consistent with the isotropic diffusion mentioned above. Fig. 8 shows the dust density at the onset of the secondary increase of ϵ_{max} . It is clear that non-linear overdensities can grow in very localized regions within the filaments. This corresponds to unstable modes with vertical wavenumbers $k_z \neq 0$, which favors an SI-like instability. To confirm that the SI is definitely at work inside the filaments, we conducted a test calculation by restarting the run for $St = 0.1$ at $t = 200\Omega^{-1}$, but with the dust back-reaction onto the gas switched off. The finding of this model is that overdensities are quickly damped, which confirms the important role of the dust feedback for the formation of clumps in the filaments.

Interestingly, with respect to simulations without coagulation, we can notice that the overdensities that are produced by the SI in presence of coagulation are stronger. For $St = 0.1$ (middle-middle panel) and $St = 0.01$ (top-middle panel), models with coagulation yield $\epsilon_{max} \approx 6$ and $\epsilon_{max} \approx 0.3 - 0.35$, respectively, whereas the growth of the instability without coagulation is marginal. We argue that for this range of parameters, the SI may be assisted by dust coagulation. To support this argument, we present in Fig. 9 growth rates of the SI (upper panel) and those obtained from our linear analysis with coagulation included (bottom panel), for $St = 0.01$. For the run with $St = 0.1$ (Model E0v2S0v1c), $St = 0.01$ corresponds roughly to the value for which overdensities start to grow inside the filaments (see middle-middle panel in Fig. 1). On this plot, the red-coloured rectangular region for $\tilde{K}_x \gtrsim 100$, with $\tilde{K}_x = k_x \eta R_0$ the dimen-

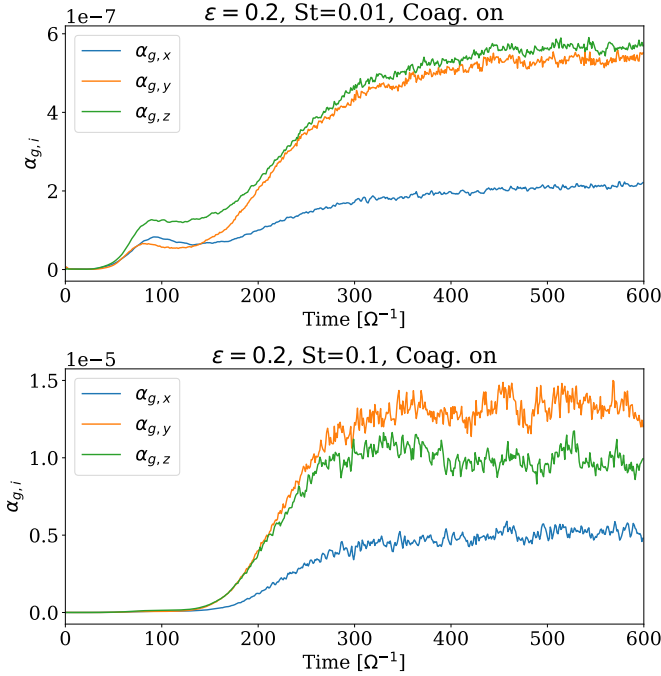


Fig. 6. For $\epsilon = 0.2$, time evolution of the dimensionless diffusion coefficients $\alpha_{g,i}$ in each direction for model E0v2S0v01c with $St = 0.01$ (top) and model E0v2S0v1c with $St = 0.1$ (bottom).

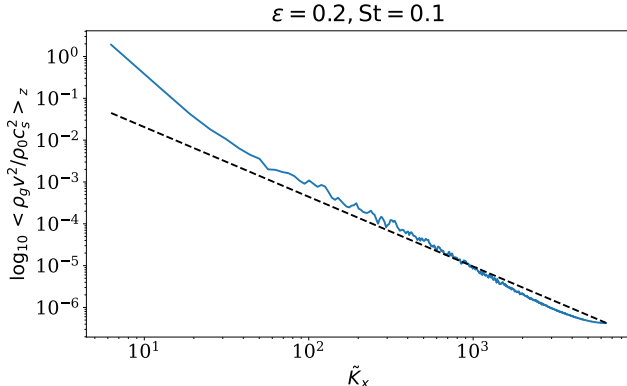


Fig. 7. Spectrum of the vertically averaged gas kinetic energy density for $\epsilon = 0.2$ and $St = 0.1$ (run E0v2S0v1c). Here, $\tilde{K}_x = k_x \eta R_0$ is the dimensionless radial wavenumber.

sionless wavenumber, corresponds to unstable CI modes as these modes have no vertical structure. The region enclosed between $10 \lesssim \tilde{K}_x \lesssim 100$ and $10 \lesssim \tilde{K}_z \lesssim 100$ can rather be identified as unstable SI modes. By comparison with the upper panel, we see that these modes have larger growth rates when coagulation is taken into account, which suggests that coagulation can amplify unstable SI modes. From Fig. 8, we estimate the typical radial extent of a vertically extended filament to be $0.02H_g$, which corresponds to $\tilde{K}_x \sim 15$. This is well inside this region of coagulation-assisted SI, confirming thereby that this mechanism can operate here.

For $St = 0.1$ (Model E0v2S0v1c), inspecting the two panels of Fig. 8 reveals that the vertical filaments broaden with time, which is simply a consequence of turbulent diffusion generated by the coagulation-assisted SI. As the filaments spread out, they can subsequently start to intersect each other, which leads to an isotropic turbulent configuration as suggested by the mid-

dle panel of Fig. 10. Note that a similar evolution is found for $St = 0.01$, for which we show in the upper panel of Fig. 10 a snapshot of the dust density when the instability has saturated.

Going back to the middle panel Fig. 10, it is interesting to note that the fully turbulent state consists of large voids and narrow particle streams, which is similar to the patterns developed by the SI for strongly coupled particles (Johansen & Youdin 2007). For standard SI, however, this regime is typically found for $\epsilon \gtrsim 1$ whereas for $\epsilon = 0.2$, dust density is left almost unchanged (see bottom panel of Fig. 10). This implies that coagulation makes this mode of nonlinear saturation of the SI occur at much lower dust-to-gas ratios. This is not surprising as coagulation tends to increase radial drift speed by increasing the Stokes number, so that growing particles can fall more rapidly through the voids created by Poisson fluctuations (Johansen & Youdin 2007). We note, however, that the dust density enhancement is limited to $\sim 30-40$ with coagulation included, whereas for standard SI this mode of nonlinear saturation generally corresponds to strong clumping with dust density enhancements $\gtrsim 100$.

4.2. Marginally coupled particles

For $\epsilon = 0.02$, the evolution outcome of the model with final Stokes number $St = 1$ and including coagulation (run E0v02s1c, bottom left panel in Fig. 1) is found to be very similar to that of $St = 0.1$ particles (run E0v02s0v1c), involving the formation of a vertically extended filament inside which CI-induced turbulence operates.

For $\epsilon = 0.2$, an interesting issue that emerges from the previous discussion in Sect. 4.1.2 is whether the conditions to reach strong clumping are less stringent with coagulation. To investigate this further, we now allow, in the case where coagulation is included, the Stokes number to increase up to $St = 1$. For standard SI, a model with $\epsilon = 0.2$ is expected to lie in the strong clumping regime for $St \sim 1$ and our main aim here is to examine if this threshold is diminished when coagulation is taken into account. In Fig. 1, models with $\epsilon = 0.2$ and $St = 1$ correspond to the bottom middle panel where we compare the runs with and without coagulation. From this plot, it is immediately evident that: i) the final outcome of the simulations does not depend on whether coagulation is included or not, and ii) including coagulation does not reduce the threshold in terms of Stokes number for the onset of strong clumping. Looking at the time evolution of ϵ_{max} for the model with coagulation, we see that the initial behaviour is consistent with the results presented in the previous section, involving increase of ϵ_{max} as coagulation-assisted SI grows and develops isotropic turbulence. At a later time $t \sim 200 \Omega^{-1}$, however, ϵ_{max} is observed to decrease before increasing again as $St \rightarrow 1$. From the time evolution of St , we estimate the (mean) Stokes number associated with the observed drop of ϵ_{max} occurring at $t \sim 200 \Omega^{-1}$ to be $St \approx 0.3$. Interestingly, we find by running simulations of standard SI with different Stokes numbers that this value coincides approximately with the one above which significant growth of the SI occurs. To explore the origin of this decrease in ϵ_{max} in more details, we have conducted a number of test calculations, by restarting the simulation with coagulation (run E0v2S1c) at $t \sim 200 \Omega^{-1}$ but with dust coagulation/feedback switched on/off. The findings of this study can be summarised as follows:

- a restarted run with dust backreaction onto the gas switched off leads to a continuous increase in ϵ_{max} due to CI, which is the opposite behaviour to that found in model E0v2S1c. This

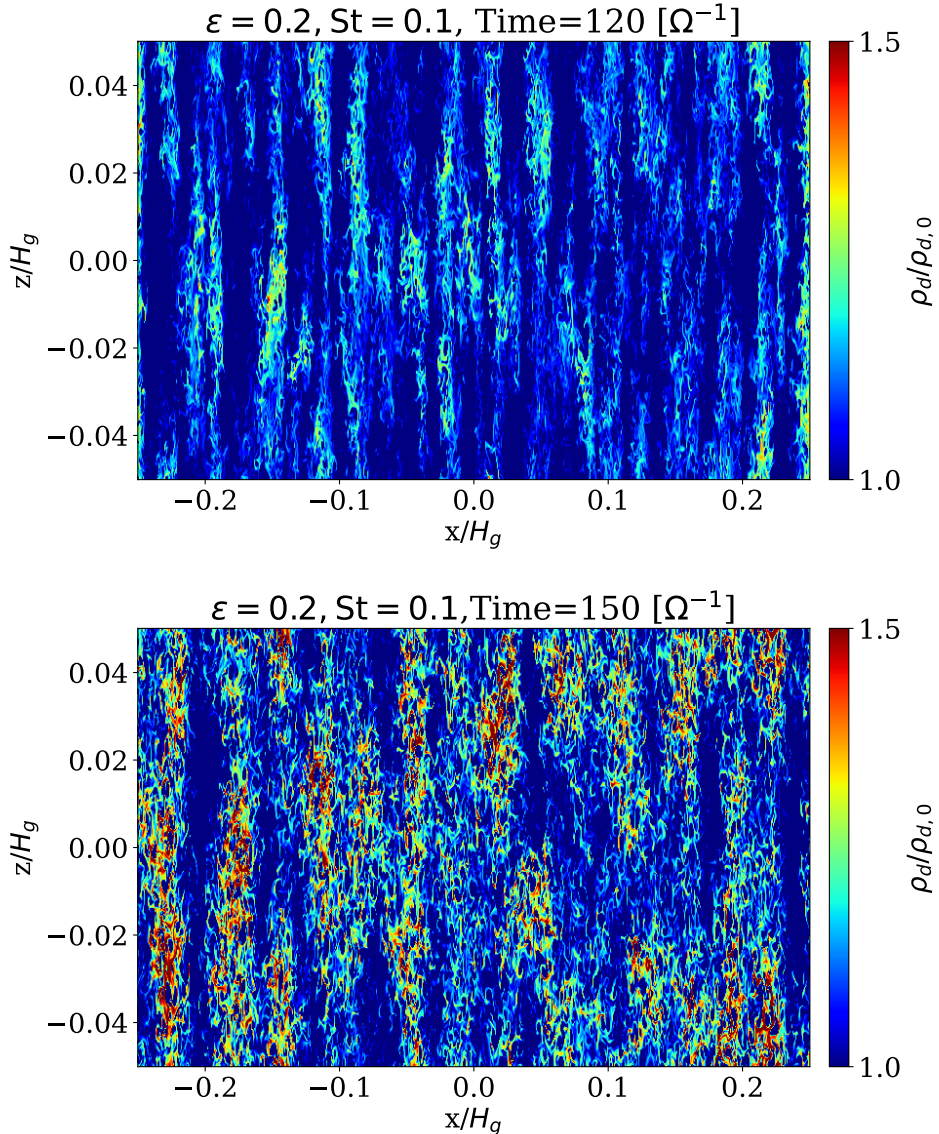


Fig. 8. For $\epsilon = 0.2$ and $St = 0.1$ (run E0v2S0v1c, with coagulation), dust density snapshots at $t = 120 \Omega^{-1}$ (left) and $t = 150 \Omega^{-1}$ (right).

demonstrates that dust feedback plays an important role in the decrease in ϵ_{max} seen in run E0v2S1c.

- a restarted run with dust coagulation switched off results in the development of the SI into stripes aligned in the vertical direction but tilted in the radial direction, similarly to the patterns formed by the SI in the case of large particles (Johansen & Youdin 2007). When applied to run E0v2S1c, this shows that from $t \sim 200 \Omega^{-1}$ onward, the SI can indeed be triggered, consistently with the results of our simulations of standard SI with various Stokes numbers. During the saturated state, we find $\epsilon_{max} \sim 0.5 - 1$ for this test calculation, which is also in agreement with our standard SI calculation with $St = 0.3$.
- a restarted run with coagulation *and* dust backreaction switched off results in a maintained quasi-stationary turbulent state, with ϵ_{max} remaining close to its initial value.

Taken together, these results suggest that provided its growth rate is high enough, the SI can counteract the effect of the CI such that the final turbulent state is similar to that found in pure SI calculations. This is illustrated in Fig. 11 which shows the evolution

of the dust density for the model with coagulation included (run E0v2S1c). The large stripes tilted toward the vertical direction that are expected to develop during nonlinear saturation of the SI for $St = 1$ particles can easily be recognized. For the particular model with $\epsilon = 0.2$ and $St = 1$, examining Table 1 confirms that the values α_{SS} and $\alpha_{g,i}$ do not depend on whether or not coagulation is included.

To clearly demonstrate the finding that the SI can overcome the effects of the CI, we show in Fig. 12 linear growth rates of the instability for $\epsilon = 0.2$ and two different values of St . Here, both the CI and SI operate, with the unstable CI (resp. SI) modes corresponding to the unstable modes that have little (resp. strong) dependence on \tilde{K}_z . We see that as coagulation proceeds and Stokes number transitions from $St = 0.3$ to $St = 1$, the maximum growth rate of the SI increases whereas unstable CI modes with radial wavenumbers in the range $\tilde{K}_x \in [5 - 100]$ are damped. This possibly arises because both CI and SI are driven by the radial drift of dust, which acts as a finite energy reservoir for the two instabilities such that any of these two instabilities can only grow at the expense of the other.

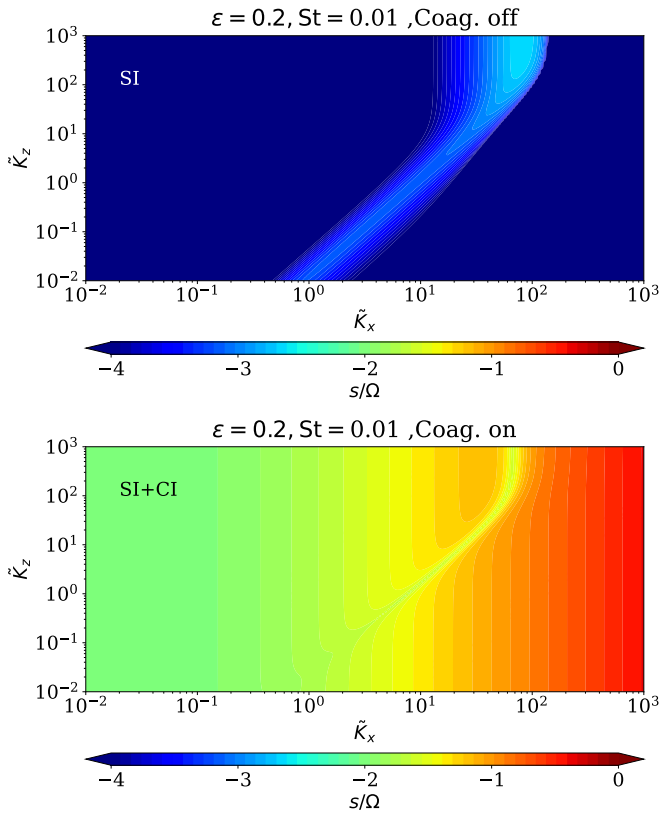


Fig. 9. Linear growth rates obtained from the linear analysis presented in Appendix A for $\epsilon = 0.2$ and $St = 0.01$ for the case without coagulation (top) and with coagulation (bottom). Here, $\tilde{K}_{x,z} = k_{x,z} \eta R_0$ are the dimensionless wavenumbers.

5. Discussion

5.1. Impact of coagulation on the Streaming Instability

Although a model with $\epsilon = 0.2$ and $St = 1$ leads to strong clumping, consistently with the results of Johansen & Youdin (2007), a necessary condition for particle clumping through the SI is generally approximated as $\epsilon \gtrsim 1$ in the disc midplane, due to the strong increase in the SI linear growth rates at $\epsilon \approx 1$ for $St \lesssim 1$. The right panels of Fig. 1 show the effect of coagulation on the SI for $\epsilon = 3$. The SI linear growth rate for $St = 0.01$ is $\sigma \sim \Omega^{-1}$ but this case only produced modest overdensities, whereas strong clumping occurred for $St \gtrsim 0.1$, as expected. Clearly, the effect of coagulation appears to be negligible for $\epsilon = 3$, regardless the (final) value for St . Combined with our results for $\epsilon = 0.2$ and $St = 1$, this suggests that for the optimally dust sizes and dust-to-gas ratios that maximize the SI growth rate, coagulation has an almost null effect. In that case, this means not only that i) coagulation has no impact on the SI linear growth rate but also that ii) the dust concentration at saturation is not affected by coagulation. Physically, this arises simply when the coagulation timescale is longer than the SI growth timescale, or equivalently when the particule coagulation growth rate is smaller than the SI growth rate. From Eq. 8, the inverse of the coagulation timescale is approximately given by:

$$t_{\text{coag}}^{-1} = \frac{1}{2} \sqrt{\frac{\pi \alpha C}{8 St}} \epsilon. \quad (26)$$

For $St = 0.01$ this leads to $t_{\text{coag}}^{-1} \sim 0.01 \Omega^{-1}$, which is indeed smaller than the aforementioned SI growth rate. Starting from

an initial Stokes number $St = 10^{-3}$, coagulation can of course promote SI by increasing the average dust size by 1-2 orders of magnitude, consistently with the results of Ho et al. (2024), but we find that once the SI is triggered, its dynamics dominate over coagulation effects.

5.2. Effect of coagulation on turbulence and dust diffusion

Nevertheless, we have also shown that under certain conditions, coagulation and SI can act in concert. This is particularly true in dust-poor discs where the SI can grow in the vertically extended filaments formed by the CI, leading to a regime of coagulation-assisted SI that ultimately results in a level of turbulence much higher compared to standard SI (see Sect. 4.1.2). For each model, the α_{SS} dimensionless parameter that quantifies the radial flux of gas orbital momentum is listed in the first column of Table 1. Most runs have $\alpha_{SS} < 0$, in agreement with previous estimations of the flux of angular momentum in SI-driven turbulent discs (Johansen & Youdin 2007; Hsu & Lin 2022). The fact that α_{SS} is more negative when coagulation is taken into account suggests that the radial transport of angular momentum induced by the CI is also inward. This is not surprising since, similarly to the SI (Johansen & Youdin 2007), CI is also powered by a global pressure gradient.

An interesting issue that needs to be investigated is how the collision velocity resulting from the turbulence compares with the fragmentation velocity v_f . It can indeed not be excluded that the turbulence driven by the coagulation and streaming instabilities in turn hinders further coagulation by producing collision velocities that exceed the fragmentation threshold. To address this question, one can estimate the maximum Stokes number St_f achievable through coagulation. From Eq. 9, it is straightforward to show that St_f is given by:

$$St_f = \frac{v_f^2}{C \alpha_{SS} c_s^2} \quad (27)$$

The fragmentation velocity has been studied both numerically and experimentally (Blum & Wurm 2008; Zsom et al. 2010; Wada et al. 2013; Gundlach & Blum 2015; Ueda et al. 2019), and is estimated to be between 1 and 10 m.s^{-1} for silicate particles and between 10 and 80 m.s^{-1} for icy aggregates. Regardless the nature of dust aggregates, all but one simulations resulted in turbulent collision velocities smaller than v_f for typical disc parameters. Assuming that R_0 corresponds to 1 AU, Model E0v2S0v1c which enters the regime of coagulation-assisted SI is the only exception, as we find $St_f \approx 0.07$ for $v_f = 1 \text{ m.s}^{-1}$. By preventing the formation of large dust grains, this implies that coagulation-driven turbulence may in that case inhibit the strong clumping phase of the SI.

A related effect of coagulation is the vertical diffusion of particles driven by the CI and/or SI. At steady-state, namely once turbulent diffusion counterbalances gravitational settling, it is expected that the particle vertical profile is characterized by a dust scale height H_d given by (Dubrulle et al. 1995; Youdin & Lithwick 2007):

$$\frac{H_d}{H_g} = \sqrt{\frac{\alpha_{g,z}}{\alpha_{g,z} + St}} \quad (28)$$

Using the values for $\alpha_{g,z}$ reported in Table 1, we find that it is possible to differentiate between CI and SI in dust-poor discs with $\epsilon \lesssim 0.2$ and for tightly coupled particles with $St \lesssim 0.1$, as the SI is ineffective at producing a significant level of turbulence under these conditions. By contrast, the CI on its own can

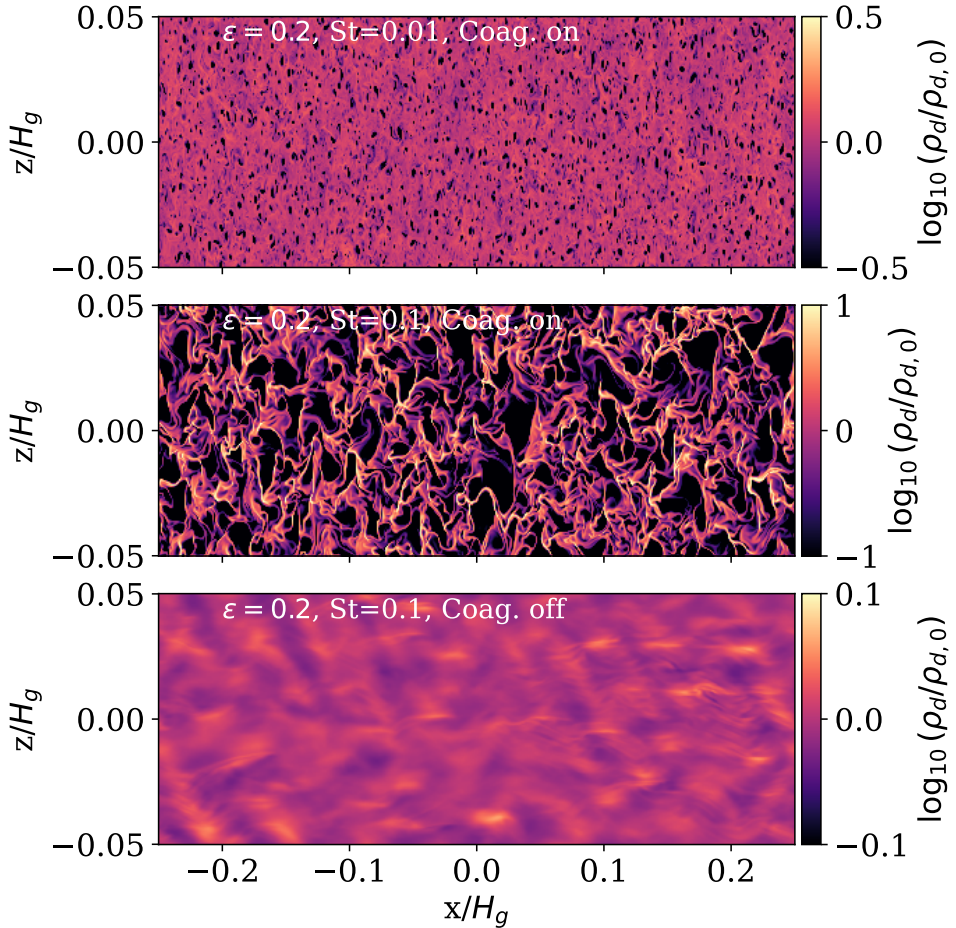


Fig. 10. From top to bottom: dust density map during the saturation phase for model E0v2S0v01c ($\epsilon = 0.2$, $St = 0.01$, with coagulation), model E0v2S0v1c ($\epsilon = 0.2$, $St = 0.1$, with coagulation), model E0v2S0v1 ($\epsilon = 0.2$, $St = 0.1$, without coagulation).

generate a vertical bulk diffusion coefficient $\alpha_{gz} \sim 5 \times 10^{-7}$ for $\epsilon = 0.02$, which results in $H_d \sim 0.006H_g$. In the coagulation-assisted SI regime (run E0v2S0v1c), α_{gz} can even reach $O(10^{-4})$ for $St = 0.1$, corresponding to $H_d \sim 0.01H_g$.

5.3. Caveats

The results that we presented in this work may suffer from a number of assumptions and limitations, the main one being that we adopted a moment equation to describe dust coagulation, based on the vertically integrated Smoluchowski equation (Sato et al. 2016; Tominaga et al. 2021). Rather than focusing on the evolution of the full dust size distribution, this approach consists in following the evolution of the so-called peak mass which represents the weighted average mass. Sato et al. (2016) have shown that provided the effect of finite size dispersion is taken into account when evaluating the collision velocities, good agreement is obtained between single-size and full size calculations of drifting and growing dust grains in protoplanetary discs. We caution, however, that the original model of Sato et al. (2016) does not take into account the effect of fragmentation and it is not clear whether or not the single-size approximation would still hold when fragmentation is considered, since this process would tend to broaden the initial dust size distribution. Relaxing the single-size approximation and considering a full, possibly wide, dust size distribution produced by fragmentation may have important

consequences on our results. In the context of the SI, recent studies have indeed shown that taking into account the effect of a dust size distribution can significantly modify the growth rate of (monodisperse) SI (Krapp et al. 2019; Paardekooper et al. 2020; Zhu & Yang 2021; McNally et al. 2021). Therefore, our model cannot explore the effect of coagulation on this "polydisperse" SI, and this should be examined in a future study.

We have also considered inviscid discs, while various hydrodynamical instabilities can be triggered in the planet-forming regions of protoplanetary discs. This gives rise to turbulence, with a corresponding turbulent viscosity such that $\alpha_{SS} \sim 10^{-4}$ typically. These levels of external turbulence may significantly impact the non-linear evolution of both the SI (Chen & Lin 2020), and CI (Tominaga et al. 2021). Although models including dissipation effects should be explored in more details, we present in App. B the results of a few viscous simulations that also take into account dust diffusion. These suggest that for the results presented in this paper may be affected by the external turbulence for $\alpha_{SS} \gtrsim 10^{-6}$.

Another limitation resides in the size of our vertical domain which, from the discussion in Sect. 5.2, is systematically higher than the dust layer thickness. The consequence is that the effects of stratification may be important and these should be examined in more details in a future study. Another reason for considering vertically stratified discs is that the CI is characterised by verti-

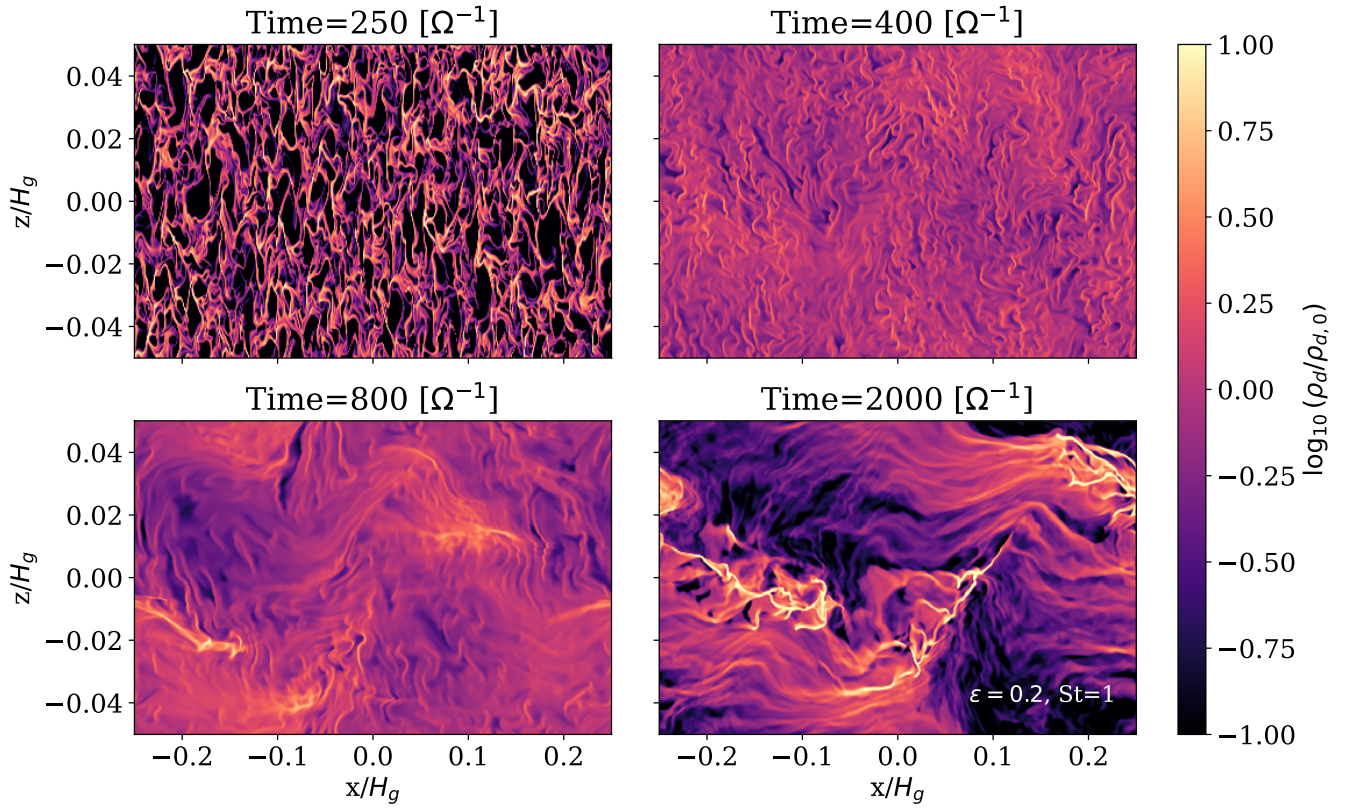


Fig. 11. For $\epsilon = 0.2$ and $St = 1$ (model E0v2S1c, with coagulation), dust density snapshots taken at different times.

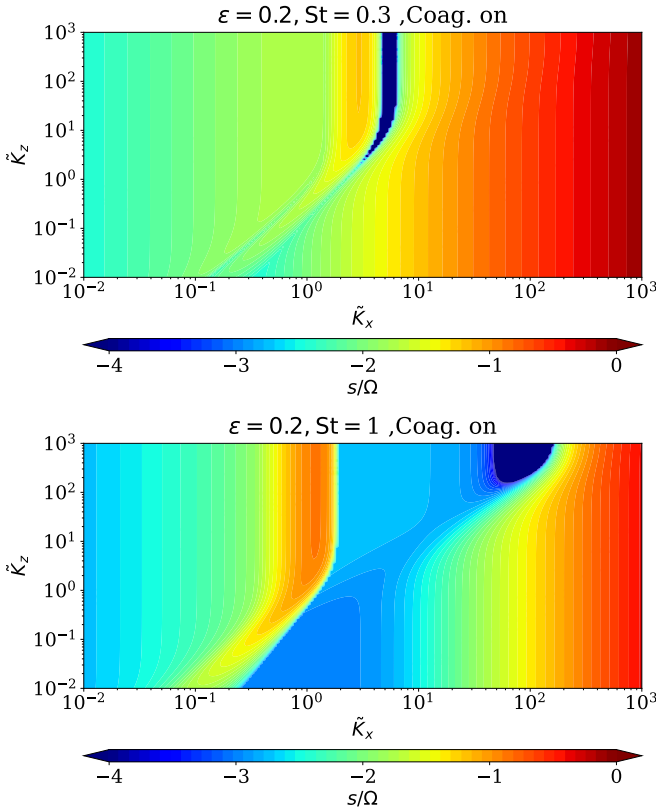


Fig. 12. For $\epsilon = 0.2$ and with the effects of coagulation included, linear growth rates obtained from the linear analysis presented in Appendix A for $St = 0.3$ (top) and $St = 1$ (bottom). Here, $\tilde{K}_{x,z} = k_{x,z} \eta R_0$ are the dimensionless wavenumbers.

cally extended filaments and it is not clear whether or not these would persist in stratified models.

We note that these two aspects, namely, considering a full dust size distribution and vertical stratification, have been recently studied by Ho et al. (2024). Although the potential important effect of the CI was not investigated in this work, they found that the dust size distribution can be significantly altered by coagulation within the dense dust clumps that are formed as the dust settles toward the midplane and the SI is triggered.

6. Summary

In this paper, we have presented the results of unstratified, axisymmetric, shearing-box simulations of streaming instability (SI) including the effect of dust coagulation. We solved a simplified version of the coagulation equation by a moment method, which consists in following the size evolution of solids that dominate the total dust surface density. Our primary aim was to examine to what extent dust growth impacts the linear growth of the SI, and to get insight into its impact on the nonlinear saturation phase of the SI. We are particularly interested in the role played by the coagulation instability (CI, Tominaga et al. (2021)), which results from the dust-density dependence of coagulation efficiency and the grain size dependence of radial drift speed. Our motivation stems from the fact that the CI can be triggered for dust-to-gas ratios as small as $\epsilon \sim 10^{-3}$ and make the Stokes number of solids rapidly reach unity, leading thereby to optimal conditions for efficient growth of the SI. We studied how the CI and the SI can interact with each other, and how the interplay between these two instabilities depends on the initial dust-to-gas ratio and on the maximum Stokes number St allowed before fragmentation sets in. Our key findings are summarized as follows:

1. In dust-poor discs with $\epsilon \sim 10^{-2}$ and for tightly coupled particles with $St \lesssim 10^{-1}$, we find that the evolution is mainly driven by the CI. Since the latter instability is by essence an axisymmetric instability, early evolution involves the formation of vertically extended filaments that tend to merge themselves more rapidly for larger Stokes numbers. Within the filaments, nonlinear saturation of the CI gives rise to anisotropic turbulence with an enhanced dust diffusion coefficient in the vertical direction.
2. In dust-rich discs with $\epsilon > 1$, the evolution is mainly driven by the SI simply because in that case, the growth timescale of the SI is smaller than the coagulation timescale. In this regime, coagulation is observed to have only little effect, not only on the initial linear growth rate of the instability, but also on the final dust concentration values reached once the SI has saturated.
3. For intermediate dust-to-gas ratios $\epsilon \sim 0.1$ and Stokes numbers $St \lesssim 0.1$, we observe the onset of the SI within the filaments formed originally by the CI. Examination of linear growth rate maps indicates that for this range of parameters, the linear growth rate of the SI is significantly increased by coagulation effects, which we refer to as a regime of coagulation-assisted SI. In this regime, nonlinear evolution leads to isotropic turbulence with dust diffusion coefficients having similar value in each direction. The generated turbulence causes the vertically extended filaments to spread out until they start to intersect each other, leading ultimately to a turbulent state characterised by large voids and narrow particle streams. The patterns that develop look similar to those formed by the SI in the strong clumping regime, albeit with a smaller dust concentration, of order $O(30 - 40)$, compared to that typical of the strong clumping regime.
4. As the Stokes number increases and approaches unity, however, SI can overcome the effect of the CI such that the final turbulent state is very similar to that found in pure SI calculations without the effect of coagulation included.

Taken together, these findings suggest that the formation of dense clumps through the SI may be rendered easier by coagulation, simply because the process of dust growth enables the SI to reside in a regime where it can operate efficiently. The CI by itself has only little impact on the onset of the SI, but it can nonetheless be a non negligible source of turbulence in protoplanetary discs, especially when it can act in concert with the SI.

Acknowledgements. Computer time for this study was provided by the computing facilities MCIA (Mésocentre de Calcul Intensif Aquitain) of the Université de Bordeaux and by HPC resources of Cines under the allocation A0170406957 made by GENCI (Grand Equipement National de Calcul Intensif). MKL is supported by the National Science and Technology Council (grants 113-2112-M-001-036-, 114-2112-M-001-018-, 113-2124-M-002-003-, 114-2124-M-002-003-) and an Académie Sinica Career Development Award (AS-CDA-110-M06). This work was partly supported by the "Action Thématische de Physique Stellaire" (ATPS) of CNRS/INSU PN Astro co-funded by CEA and CNES, and by ORCHID program (project number: 49523PG, co-PI: Dutrey-Tang), funded by the French Ministry for Europe and Foreign Affairs, the French Ministry for Higher Education and Research and the National Science and Technology Council (NSTC).

Carrera, D., Lim, J., Eriksson, L. E. J., Lyra, W., & Simon, J. B. 2025, A&A, 696, L23
 Chen, K. & Lin, M.-K. 2020, ApJ, 891, 132
 Drążkowska, J. & Dullemond, C. P. 2014, A&A, 572, A78
 Dubrulle, B., Morfill, G., & Sterzik, M. 1995, Icarus, 114, 237
 Dullemond, C. P. & Dominik, C. 2005, A&A, 434, 971
 Fromang, S. & Papaloizou, J. 2006, A&A, 452, 751
 Gundlach, B. & Blum, J. 2015, ApJ, 798, 34
 Ho, K. W., Li, H., & Li, S. 2024, ApJ, 975, L34
 Hsu, C.-Y. & Lin, M.-K. 2022, ApJ, 937, 55
 Johansen, A. & Youdin, A. 2007, ApJ, 662, 627
 Johansen, A., Youdin, A., & Mac Low, M.-M. 2009, ApJ, 704, L75
 Krapp, L., Benítez-Llambay, P., Gressel, O., & Pessah, M. E. 2019, ApJ, 878, L30
 Li, R. & Youdin, A. N. 2021, ApJ, 919, 107
 Lin, M.-K. & Youdin, A. N. 2017, ApJ, 849, 129
 McNally, C. P., Lovascio, F., & Paardekooper, S.-J. 2021, MNRAS, 502, 1469
 Nakagawa, Y., Sekiya, M., & Hayashi, C. 1986, Icarus, 67, 375
 Ormel, C. W. & Cuzzi, J. N. 2007, A&A, 466, 413
 Paardekooper, S.-J., McNally, C. P., & Lovascio, F. 2020, MNRAS, 499, 4223
 Sato, T., Okuzumi, S., & Ida, S. 2016, A&A, 589, A15
 Shakura, N. I. & Sunyaev, R. A. 1973, A&A, 24, 337
 Simon, J. B., Armitage, P. J., Li, R., & Youdin, A. N. 2016, ApJ, 822, 55
 Tominaga, R. T., Inutsuka, S.-i., & Kobayashi, H. 2021, ApJ, 923, 34
 Tominaga, R. T., Kobayashi, H., & Inutsuka, S.-i. 2022a, ApJ, 937, 21
 Tominaga, R. T. & Tanaka, H. 2023, ApJ, 958, 168
 Tominaga, R. T. & Tanaka, H. 2025, ApJ, 983, 15
 Tominaga, R. T., Tanaka, H., Kobayashi, H., & Inutsuka, S.-i. 2022b, ApJ, 940, 152
 Ueda, T., Flock, M., & Okuzumi, S. 2019, ApJ, 871, 10
 Wada, K., Tanaka, H., Okuzumi, S., et al. 2013, A&A, 559, A62
 Yang, C.-C., Johansen, A., & Carrera, D. 2017, A&A, 606, A80
 Yang, C.-C., Mac Low, M.-M., & Johansen, A. 2018, ApJ, 868, 27
 Youdin, A. & Johansen, A. 2007, ApJ, 662, 613
 Youdin, A. N. & Goodman, J. 2005, ApJ, 620, 459
 Youdin, A. N. & Lithwick, Y. 2007, Icarus, 192, 588
 Zhu, Z. & Yang, C.-C. 2021, MNRAS, 501, 467
 Zsom, A., Ormel, C. W., Gütter, C., Blum, J., & Dullemond, C. P. 2010, A&A, 513, A57

References

Abod, C. P., Simon, J. B., Li, R., et al. 2019, ApJ, 883, 192
 Benítez-Llambay, P., Krapp, L., & Pessah, M. E. 2019, ApJS, 241, 25
 Benítez-Llambay, P. & Masset, F. S. 2016, ApJS, 223, 11
 Blum, J. & Wurm, G. 2008, ARA&A, 46, 21
 Carrera, D., Johansen, A., & Davies, M. B. 2015, A&A, 579, A43

Appendix A: Linearized equations

In order to linearize equations Eqs. 1–4, we write X as a quantity of the system as the sum between the equilibrium state X_0 (Eqs. 11–14), and a perturbation $\delta X \ll X_0$ in Fourier modes with k_x and k_z the spatial modes and σ the growth rate of the instability.

$$X(x, z, t) = X_0(x, z) + \delta X \times e^{i(k_x x + k_z z) + \sigma t} \quad (\text{A.1})$$

By injecting this into the mass continuity equations Eq. 1 and Eq. 3, we obtain

$$\sigma \delta \rho_g = -\rho_{g,0} (ik_x \delta u_x + ik_z \delta u_z) - ik_x u_{x,0} \delta \rho_g \quad (\text{A.2a})$$

$$\sigma \delta \rho_d = -\rho_{d,0} (ik_x \delta v_x + ik_z \delta v_z) - ik_x v_{x,0} \delta \rho_d \quad (\text{A.2b})$$

$$- \rho_{d,0} D (k_x^2 + k_z^2) (\delta \rho_d / \rho_{d,0} - \delta \rho_g / \rho_{g,0})$$

Similarly, with the equations of conservation of momentum for the gas Eq. 2

$$\begin{aligned} \sigma \delta u_x &= -u_{x,0} ik_x \delta u_x + 2\Omega \delta u_y - c_s^2 ik_x \frac{\delta \rho_g}{\rho_{g,0}} + \delta F_x^{visc} \\ &\quad - C_{DF} m_p^{-1/3} \left\{ [\delta \rho_d - \frac{1}{3m_p} \rho_d \delta m_p] (u_{x,0} - v_{x,0}) \right. \\ &\quad \left. + \rho_d (\delta u_x - \delta v_x) \right\} \end{aligned} \quad (\text{A.3a})$$

$$\begin{aligned} \sigma \delta u_y &= -u_{x,0} ik_x \delta u_y - \frac{1}{2} \Omega \delta u_x + \delta F_y^{visc} \\ &\quad - C_{DF} m_p^{-1/3} \left\{ [\delta \rho_d - \frac{1}{3m_p} \rho_d \delta m_p] (u_{y,0} - v_{y,0}) \right. \\ &\quad \left. + \rho_d (\delta u_y - \delta v_y) \right\} \end{aligned} \quad (\text{A.3b})$$

$$\begin{aligned} \sigma \delta u_z &= -u_{x,0} ik_x \delta u_z - c_s^2 ik_z \frac{\delta \rho_g}{\rho_{g,0}} + \delta F_z^{visc} \\ &\quad - C_{DF} m_p^{-1/3} \rho_d (\delta u_z - \delta v_z) \end{aligned} \quad (\text{A.3c})$$

with $C_{DF} = \Omega \sqrt{\frac{8}{\pi} \frac{H_g}{\rho_i} (\frac{4\pi\rho_i}{3})^{1/3}}$ a coefficient related to drag force and $\delta F_{(x,y,z)}^{visc}$ the linearized viscous forces from Chen & Lin (2020):

$$\delta F_x^{visc} = -v(k_z^2 + \frac{4}{3} k_x^2) \delta v_x - \frac{1}{3} v k_x k_z \delta v_z \quad (\text{A.4a})$$

$$\delta F_y^{visc} = -v(k_z^2 + k_x^2) \delta v_y \quad (\text{A.4b})$$

$$\delta F_z^{visc} = -v(\frac{4}{3} k_z^2 + k_x^2) \delta v_z - \frac{1}{3} v k_x k_z \delta v_x \quad (\text{A.4c})$$

and for the equations of conservation of momentum for the dust Eq. 4,

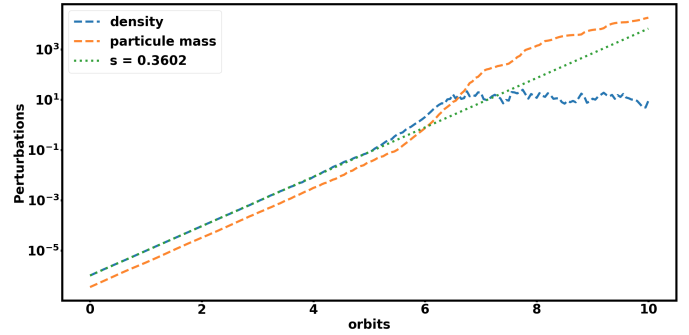


Fig. A.1. In blue and orange, the perturbation $\frac{\max(|\rho_d - \rho_{d,0}|)}{\rho_{d,0}}$ and $\frac{\max(|m_p - m_{p,0}|)}{m_{p,0}}$ obtained through hydrodynamic simulations with coagulation. In green, the theoretical growth rate obtained analytically.

$$\sigma \delta v_x = -v_{x,0} ik_x \delta v_x + 2\Omega \delta v_y - C_{DF} m_p^{-1/3} \left\{ [\delta \rho_g - \frac{1}{3m_p} \rho_g \delta m_p] (v_{x,0} - u_{x,0}) \right. \quad (\text{A.5a})$$

$$\left. + \rho_g (\delta v_x - \delta u_x) \right\}$$

$$\sigma \delta v_y = -v_{x,0} ik_x \delta v_y - \frac{1}{2} \Omega \delta v_x - C_{DF} m_p^{-1/3} \left\{ [\delta \rho_g - \frac{1}{3m_p} \rho_g \delta m_p] (v_{y,0} - u_{y,0}) \right. \quad (\text{A.5b})$$

$$\left. + \rho_g (\delta v_y - \delta u_y) \right\}$$

$$\sigma \delta v_z = -v_{x,0} ik_x \delta v_z - C_{DF} m_p^{-1/3} \rho_g (\delta v_z - \delta u_z) \quad (\text{A.5c})$$

And finally, the perturbed equation for the coagulation equation Eq. 8

$$\sigma \delta m_p = -v_{x,0} ik_x \delta m_p + D_{coag} m_p^{5/6} \rho_g^{-1/2} \rho_d \left[\frac{5}{6} \frac{\delta m_p}{m_p} - \frac{1}{2} \frac{\delta \rho_g}{\rho_g} + \frac{\delta \rho_d}{\rho_d} \right] \quad (\text{A.6})$$

$$\text{with } D_{coag} = \left(\frac{\pi}{2} \right)^{5/12} \times 3^{5/6} \rho_i^{-1/3} \sqrt{2.3\alpha} H_g^{-1/2} c_s.$$

This system of 9 equations is rewritten in its matrix form as $s\mathbf{V} = A\mathbf{V}$, using the dimensionless quantities $\hat{v} = \frac{v}{\eta R \Omega}$, $K = k\eta R$ and $s = \frac{\sigma}{\Omega}$, with the perturbation vector $\mathbf{V} = \left[\frac{\delta \rho_g}{\rho_g}, \frac{\delta \rho_d}{\rho_d}, \delta \hat{u}_x, \delta \hat{u}_y, \delta \hat{u}_z, \delta \hat{v}_x, \delta \hat{v}_y, \delta \hat{v}_z, \frac{\delta m_p}{m_p} \right]^\top$ and the matrix of the linearized system A .

For a given spatial mode (K_x, K_z) , the largest eigenvalue of A corresponds to the growth rate σ of the most unstable mode, while the associated eigenvector can be used to study the linear case of this mode numerically. This allows verification of the coagulation implementation as well as the analytical development growth rates derived from the matrix's eigenvalues by comparing the two, done Figure A.1 in the linA case $St = 0.1$, $\epsilon = 3$ and $(K_x, K_z) = (30, 30)$ with coagulation. The analytical solution gives $s = 0.3602$, identical to the numerical growth rate derived from the particle density and particle mass until the perturbation is no longer negligible ($\delta X \sim 0.1$).

Appendix B: Effect of gas viscosity and dust diffusion

In the inviscid limit that we considered in this work, the numerical dissipation may impact our results, such that these could be dependent on the employed resolution. This is because the growth rate of CI increases with radial wavenumber, such that the maximum wavenumber that is resolved by the grid is expected to be unstable. Here, we present the results of additional simulations with non-zero gas viscosity, parameterized as $\nu = \alpha c_S H_g$, and with dust diffusion coefficient set to the same value $D = \nu$. As in inviscid simulations presented above, the α_{coag} parameter entering in Eq. 9 is set to $\alpha_{\text{coag}} = 10^{-4}$. The aim is to examine i) how the results are changed when dissipation processes are controlled and ii) how these would be modified in presence of external turbulence, namely when the turbulence originates from other sources of instabilities than the CI and/or SI themselves. For different values of standard α parameter, the time evolution of ϵ_{max} and St for these runs is presented in Fig. B.1. Not surprisingly, the linear growth rate of the instabilities is reduced as α is increased. This is a consequence of the stabilization of the coagulation instability by dust diffusion (Tom-inaga et al. 2021). Unstable high wavenumbers modes are also suppressed, as illustrated by Fig. B.2 which shows the dust density at the end of the linear growth phase. From Fig. B.1, we estimate the value for the numerical viscosity to correspond to $\alpha \sim 10^{-9} - 10^{-7}$. This is in line with the expectation that unstable modes with wavenumbers such that $kH \sim 1/\sqrt{\alpha}$ are damped by turbulence (Dubrulle et al. 1995). Using $\alpha = 10^{-7}$, this gives $kH \approx 3 \times 10^3$, which is close to the value mentioned in Sect. 4.1.1. Going back to Fig. B.1, we observe growth of the SI for each value of α we considered, except for $\alpha = 10^{-6}$. In that case, however, $St \lesssim 0.5$ at the end of the simulation due to slower coagulation, leading to a reduced SI growth rate. As $St \rightarrow 1$, the SI should nevertheless enter a strong clumping regime, as it is expected in that case the SI growth rate to be only impacted by diffusion for $\alpha = 10^{-6}$ (e.g. Figure 3. of Chen & Lin (2020), upper left panel).

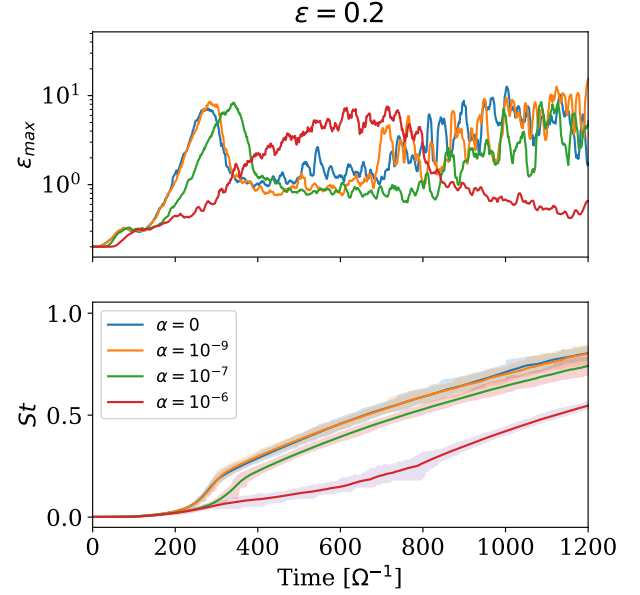


Fig. B.1. For $\epsilon = 0.2$, $St = 1$ and with coagulation included, time evolution of the maximum dust-to-gas ratio ϵ_{max} and Stokes number St in viscous simulations where the α viscous stress parameter is taken to be equal to the dimensionless dust diffusion coefficient.

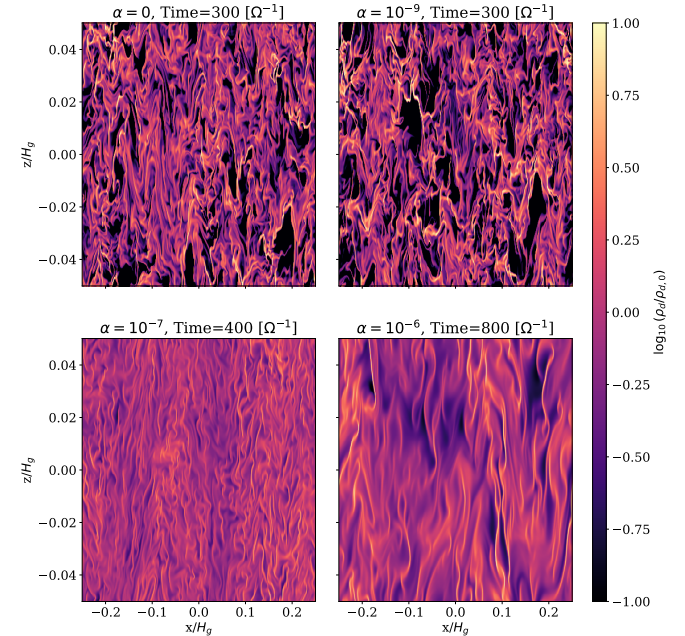


Fig. B.2. For $\epsilon = 0.2$, $St = 1$, dust density snapshots for the reference inviscid run (top left) and for viscous simulations with $\alpha = 10^{-9}$ (top right), $\alpha = 10^{-7}$ (bottom left), and $\alpha = 10^{-6}$ (bottom right).